frontiers | Frontiers in Physics

TYPE Review
PUBLISHED 28 October 2024
DOI 10.3389/fphy.2024.1487314

OPEN ACCESS

EDITED BY
Oscar Moreno,
Complutense University of Madrid, Spain

REVIEWED BY
Francesco Giovanni Celiberto,
University of Alcalá, Spain
Shuichiro EBATA,
Saitama University, Japan

*CORRESPONDENCE
M. C. Atkinson,
mackenzie.c.atkinson@gmail.com

RECEIVED 27 August 2024
ACCEPTED 30 September 2024
PUBLISHED 28 October 2024

CITATION
Atkinson MC and Dickhoff WH (2024) Neutron skins: A perspective from dispersive optical models.
Front. Phys. 12:1487314.
doi: 10.3389/fphy.2024.1487314

Neutron skins: A perspective from dispersive optical models

M. C. Atkinson[1]* and W. H. Dickhoff[2]

[1]Lawrence Livermore National Laboratory, Livermore, CA, United States, [2]Department of Physics, Washington University in St. Louis, St. Louis, MO, United States

An overview of neutron skin predictions obtained using an empirical nonlocal dispersive optical model (DOM) is presented. The DOM links both scattering and bound-state experimental data through a subtracted dispersion relation which allows for fully consistent, data-informed predictions for nuclei where such data exist. Large skins were predicted for both ^{48}Ca ($R^{48}_{\rm skin}$ = 0.25 ± 0.023 fm in 2017) and ^{208}Pb ($R^{208}_{\rm skin}$ = 0.25 ± 0.05 fm in 2020). Whereas the DOM prediction in ^{208}Pb is within 1σ of the subsequent PREX-2 measurement, the DOM prediction in ^{48}Ca is over 2σ larger than the thin neutron skin resulting from CREX. From the moment it was revealed, the thin skin in ^{48}Ca has puzzled the nuclear-physics community as no adequate theories simultaneously predict both a large skin in ^{208}Pb and a small skin in ^{48}Ca. The DOM is unique in its ability to treat both structure and reaction data on the same footing, providing a unique perspective on this $R_{\rm skin}$ puzzle. It appears vital that more neutron data be measured in both the scattering and bound-state domain for ^{48}Ca to clarify the situation.

KEYWORDS

neutron skin, structure, reactions, optical potential, Green's function

1 Introduction

A fundamental question in nuclear physics is how the constituent neutrons and protons are distributed in the nucleus. In particular, for a nucleus which has a substantial excess of neutrons over protons, are the extra neutrons distributed evenly over the nuclear volume or are these excess neutrons localized in the periphery of the nucleus forming a neutron skin? A quantitative measure is provided by the neutron-skin thickness, $R_{\rm skin}$, defined as the difference between the point neutron and proton root-mean-squared (RMS) radii, that is, $R_{\rm skin} = R_n - R_p$.

The nuclear symmetry energy, which characterizes the variation of the binding energy as a function of neutron–proton asymmetry, opposes the creation of nuclear matter with excesses of either type of nucleon. The extent of the neutron skin is determined by the relative strengths of the symmetry energy between the central near-saturation and peripheral less-dense regions. Therefore, $R_{\rm skin}$ is a measure of the density dependence of the symmetry energy around saturation [1–4]. This dependence is very important for determining many nuclear properties, including masses, radii, and the location of drip lines in the chart of nuclides. Its importance extends to astrophysics for understanding supernovae and neutron stars [5, 6], and to heavy-ion reactions [7].

Given the rich physics packed in this observable, a large number of studies (both experimental and theoretical) have been devoted to determining neutron skins [8, 9]. Whereas R_p is extracted quite accurately from elastic electron scattering cross sections (through the charge form factor, $F_{\rm ch}$) [10] or laser spectroscopy [11], most experimental determinations of R_n are model dependent [8]. The neutron skin can be determined with essentially the same degree of model independence as $F_{\rm ch}$ through parity-violating electron scattering [9, 12]. The parity-violating asymmetries are governed by the weak form factor,

F_W, which is the Fourier transform of the weak distribution. The weak distribution is predominantly determined by the neutron distribution, owing to the weak charge of the neutron being of order 1 and that of the proton being nearly 0. The first parity-violating experiment performed by the PREX collaboration at Jefferson Lab yielded a thick neutron skin of ^{208}Pb with a rather large uncertainty [13]. A second experiment, dubbed PREX-2, was later performed, resulting in a ^{208}Pb skin of $R^{208}_{\rm skin} = 0.283 \pm 0.071$ fm [14]. The following year, the CREX experiment extracted a much smaller skin in ^{48}Ca of $R^{48}_{\rm skin} = 0.121 \pm 0.026\,(\rm exp) \pm 0.024\,(\rm model)$ fm [15]. The large difference between the measured neutron skins in ^{48}Ca and ^{208}Pb has puzzled the nuclear-physics community since the CREX result was published.

There currently exists no theory that predicts a thick skin in ^{208}Pb and a thin skin in ^{48}Ca. All theoretical studies of these nuclei based on a mean-field approach predict a strong, positive correlation between the neutron skins of ^{208}Pb and ^{48}Ca; however, it has been argued that the large error bars for PREX-2 may not provide a stringent constraint on the isovector part of energy density functionals [16]. Separate *ab initio* approaches exist for both nuclei. In Ref. [17], a neutron skin for ^{48}Ca that is consistent with the CREX experiment was predicted, whereas the results of Refs. [18, 19] exhibit mild tension with the PREX-2 results. Furthermore, studies of the relation between neutron skins and the nuclear equation of state (EOS) conclude that these skins are tightly correlated with the slope of the symmetry energy, L, meaning that the EOS derived from the thin $R_{\rm skin}$ measured in ^{48}Ca is incompatible with the EOS derived from the thick $R_{\rm skin}$ measured in ^{208}Pb. Through this relation to the nuclear EOS, these differing neutron skin measurements even lead to tensions in exotic astrophysical systems such as neutron stars [20]. More specifically, mass–radius curves predicted from the two different $R_{\rm skin}$-derived EOS are incompatible with each other and even with observations.

In this article, we review an alternative theoretical method to predict $R_{\rm skin}$ in ^{48}Ca and ^{208}Pb. We employed a dispersive optical model (DOM) analysis of bound and scattering data to constrain the nucleon self-energies, $\Sigma_{\ell j}$, of ^{48}Ca and ^{208}Pb. The self-energy acts as a complex and phenomenological nonlocal potential that unites the nuclear structure and reaction domains [21–23] by leveraging Green's function theory. The DOM was originally developed by Mahaux and Sartor [21], employing local real and imaginary potentials connected through dispersion relations. However, only with the introduction of nonlocality can realistic self-energies be obtained [22, 23]. The Dyson equation then determines the single-particle propagator, or Green's function, $G_{\ell j}(r, r'; E)$, from which bound-state and scattering observables can be deduced. In particular, the particle number and density distributions of the nucleons can be inferred, thus enabling the investigation of neutron skins. The DOM treats both structure and reaction data on the same footing, unlike mean-field or *ab initio* approaches applied to these systems, providing a unique perspective on the $R_{\rm skin}$ puzzle revealed by experiments at Jefferson Lab.

The underlying Green's function ingredients of the single-particle propagator are presented in Section 2.1, whereas the DOM framework is introduced in Section 2.2. The DOM description of relevant experimental data for ^{48}Ca and ^{208}Pb is presented in Section 2.3. A discussion of the neutron skin results for these nuclei is given in Section 3. Conclusions and some outlook are presented in Section 4.

2 Theory

This section is organized to provide brief introductions into the underlying theory of the DOM.

2.1 Single-particle propagator

The single-particle propagator describes the probability amplitude for adding (removing) a particle in state α at one time to the ground state and propagating on top of that state until a later time when it is removed (added) in state β [24]. In addition to the conserved orbital and total angular momentum (ℓ and j, respectively), the labels α and β in Equation 1 refer to a suitably chosen single-particle basis. We employed a coordinate-space basis in our original ^{48}Ca calculation in Ref. [25] but have since updated to using a Lagrange basis [26] in all subsequent calculations (including that of ^{208}Pb from Ref. [27]). It is convenient to work with the Fourier-transformed propagator in the energy domain,

$$G_{\ell j}(\alpha,\beta;E) = \langle\Psi_0^A|a_{\alpha\ell j}\frac{1}{E-\left(\hat{H}-E_0^A\right)+i\eta}a^\dagger_{\beta\ell j}|\Psi_0^A\rangle + \langle\Psi_0^A|a^\dagger_{\beta\ell j}\frac{1}{E-\left(E_0^A-\hat{H}\right)-i\eta}a_{\alpha\ell j}|\Psi_0^A\rangle, \tag{1}$$

with E_0^A representing the energy of the non-degenerate ground state $|\Psi_0^A\rangle$. Many interactions can occur between the addition and removal of the particle (or vice versa), all of which need to be considered to calculate the propagator. No assumptions about the detailed form of the Hamiltonian $\hat{H}$ need be made for the present discussion, but it will be assumed that a meaningful Hamiltonian exists that contains two-body and three-body contributions. The application of the perturbation theory then leads to the Dyson equation [24], which is given by

$$G_{\ell j}(\alpha,\beta;E) = G^{(0)}_\ell(\alpha,\beta;E) + \sum_{\gamma,\delta} G^{(0)}_\ell(\alpha,\gamma;E)\Sigma^\star_{\ell j}(\gamma,\delta;E)G_{\ell j}(\delta,\beta;E), \tag{2}$$

where $G^{(0)}_\ell(\alpha,\beta;E)$ corresponds to the unperturbed propagator (the propagator derived from the unperturbed Hamiltonian, H_0, which in the DOM corresponds to the kinetic energy) and $\Sigma^\star_{\ell j}(\gamma,\delta;E)$ is the irreducible self-energy [24]. The hole spectral density for energies below ε_F is obtained from

$$S^h_{\ell j}(\alpha,\beta;E) = \frac{1}{\pi}\,\mathrm{Im}\,G_{\ell j}(\alpha,\beta;E), \tag{3}$$

where the h superscript signifies it is the hole spectral amplitude. For brevity, we drop this superscript for the rest of this review. The diagonal element of Equation 3 is known as the (hole) spectral function identifying the probability density for the removal of a single-particle state with quantum numbers $\alpha\ell j$ at energy E. The single-particle density distribution can be calculated from the hole spectral function in the following way,

$$\rho^{(p,n)}_{\ell j}(r) = \sum_{\ell j}(2j+1)\int_{-\infty}^{\varepsilon_F} dE\; S^{(p,n)}_{\ell j}(r,r;E), \tag{4}$$

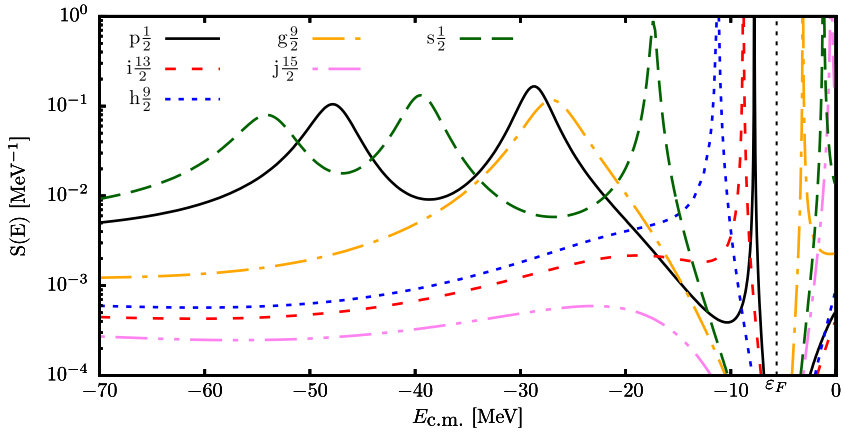

FIGURE 1
Neutron spectral functions of a representative set of ℓj shells in ^{208}Pb. The particle states are differentiated from the hole states by the vertical dashed line which corresponds to the location of the Fermi energy. Figure adapted from Ref. [30].

where the (p, n) superscript refers to protons or neutrons, and $\varepsilon_F = \frac{1}{2}(E_0^{A+1} - E_0^{A-1})$ is the average Fermi energy which separates the particle and hole domains [24]. The number of protons and neutrons (Z, N) is calculated by integrating $\rho_{\ell j}^{(p,n)}(r)$ over all space. In addition to the particle number, the total binding energy can be calculated from the hole spectral function using the Migdal–Galitski sum rule [24],

$$E_0^{N,Z} = \frac{1}{2}\sum_{\alpha\beta}\int_0^{\varepsilon_F} dE\Big[\langle\alpha|\hat{T}|\beta\rangle S^h(\alpha,\beta;E) + \delta_{\alpha\beta}ES^h(\alpha,\alpha;E)\Big]. \quad (5)$$

This expression assumes that the dominant contribution involves the two-nucleon interaction [28, 29] and the ℓj labels have been subsumed in α and β.

To visualize the spectral function of Equation 3, it is useful to sum (or integrate) over the basis variables, α, so that only energy dependence remains, $S_{\ell j}(E)$. The spectral strength $S_{\ell j}(E)$ is the contribution at energy E to the occupation from all orbitals with angular momentum ℓj. It reveals that the strength for a shell can be fragmented, rather than being isolated at the independent particle model (IPM) energy levels. Figure 1 shows the spectral strength for a representative set of neutron shells in ^{208}Pb that would be considered bound and fully occupied in the IPM. The location of the peaks in Figure 1 corresponds to the energies of discrete bound states with one nucleon removed. For example, the s1/2 spectral function in Figure 1 has four peaks, three below ε_F corresponding to the 0s1/2, 1s1/2, and 2s1/2 quasihole states, and one above ε_F corresponding to the 3s1/2 quasiparticle state. The quasihole wave functions of these bound states can be obtained by transforming the Dyson equation into a nonlocal Schrödinger-like equation by disregarding the imaginary part of $\Sigma^\star(\alpha,\beta;E)$,

$$\sum_\gamma \langle\alpha|T_\ell + \text{Re}\,\Sigma_{\ell j}^\star\left(\varepsilon_{\ell j}^n\right)|\gamma\rangle\psi_{\ell j}^n(\gamma) = \varepsilon_{\ell j}^n\psi_{\ell j}^n(\alpha), \quad (6)$$

where $\langle\alpha|T_\ell|\gamma\rangle$ is the kinetic energy matrix element, including the centrifugal term. The wave function, $\psi_{\ell j}^n(\alpha)$, is the overlap between the A and $A-1$ systems and the corresponding energy, $\varepsilon_{\ell j}^n$, is the energy required to remove a nucleon with the particular quantum numbers $n\ell j$,

$$\psi_{\ell j}^n(\alpha) = \langle\Psi_n^{A-1}|a_{\alpha\ell j}|\Psi_0^A\rangle, \qquad \varepsilon_{\ell j}^n = E_0^A - E_n^{A-1}. \quad (7)$$

When solutions to Equation 6 are found near the Fermi energy where there is naturally no imaginary part of the self-energy, the normalization of the quasihole is well defined as the spectroscopic factor,

$$\mathcal{Z}_{\ell j}^n = \left(1 - \frac{\partial\Sigma_{\ell j}^\star\left(\alpha_{qh},\alpha_{qh};E\right)}{\partial E}\bigg|_{\varepsilon_{\ell j}^n}\right)^{-1}, \quad (8)$$

where α_{qh} corresponds to the quasihole state in Equation 7. The quasihole peaks in Figure 1 get narrower as the levels approach ε_F, which is a consequence of the imaginary part of the irreducible self-energy decreasing when approaching ε_F. In fact, the last mostly occupied neutron level in Figure 1 (2p1/2) has a spectral function that is essentially a delta function peaked at its energy level, where the imaginary part of the self-energy vanishes. For these orbitals, the strength of the spectral function at the peak corresponds to the spectroscopic factor in Equation 8. The spectroscopic factor can be probed using the exclusive $(e, e'p)$ reaction which will be discussed in Section 2.4 (see also Refs. [31, 32]).

2.2 Dispersive optical model

The Dyson equation, Equation 2, simplifies the complicated task of calculating $G(\alpha,\beta;E)$ from Equation 1 to finding and inverting a suitable $\Sigma^\star(\alpha,\beta;E)$ (suppressing the ℓj labels). It was recognized long ago that $\Sigma^\star(\alpha,\beta;E)$ represents the potential that describes elastic-scattering observables [33]. The link with the potential at negative energy is then provided by the Green's function framework as was realized by Mahaux and Sartor who introduced the DOM as reviewed in Ref. [21]. The analytic structure of the nucleon self-energy allows one to apply the dispersion relation, which relates the real part of the self-energy at a given energy to a dispersion integral

of its imaginary part over all energies. The energy-independent correlated Hartree–Fock (HF) contribution [24] is removed by employing a subtracted dispersion relation with the Fermi energy used as the subtraction point [21]. The subtracted form has the further advantage that the emphasis is placed on energies closer to the Fermi energy for which more experimental data are available. The real part of the self-energy at the Fermi energy is then still referred to as the HF term and is sufficiently attractive to bind the relevant levels at about the correct energies. In practice, the imaginary part is assumed to extend to the Fermi energy on both sides while being very small in its vicinity. The subtracted form of the dispersion relation employed in this work is given by

$$\begin{aligned}\mathrm{Re}\,\Sigma^{\star}(\alpha,\beta;E) = \mathrm{Re}\,\Sigma^{\star}(\alpha,\beta;\varepsilon_F) \\ -\mathcal{P}\int_{\varepsilon_F}^{\infty}\frac{dE'}{\pi}\,\mathrm{Im}\,\Sigma^{\star}(\alpha,\beta;E')\left[\frac{1}{E-E'}-\frac{1}{\varepsilon_F-E'}\right] \\ +\mathcal{P}\int_{-\infty}^{\varepsilon_F}\frac{dE'}{\pi}\,\mathrm{Im}\,\Sigma^{\star}(\alpha,\beta;E')\left[\frac{1}{E-E'}-\frac{1}{\varepsilon_F-E'}\right],\end{aligned} \tag{9}$$

where $\mathcal{P}$ is the principal value. The static term, $\mathrm{Re}\Sigma^{\star}(\alpha,\beta;\varepsilon_F)$, is denoted by Σ_{HF} from here on. Equation 9 constrains the real part of $\Sigma^{\star}(\alpha,\beta;E)$ by empirical information of its HF and imaginary parts which are closely tied to experimental data. Initially, standard functional forms for these terms were introduced by Mahaux and Sartor who also cast the DOM potential in a local form by a standard transformation which turns a nonlocal static HF potential into an energy-dependent local potential [34]. Such an analysis was extended in Refs. [35, 36] to a sequence of Ca isotopes and in Ref. [37] to semi-closed-shell nuclei heavier than Ca. The transformation to the exclusive use of local potentials precludes a proper calculation of the nucleon particle number and expectation values of the one-body operators, like the charge density in the ground state (see Equation 4). This obstacle was eliminated in Ref. [38], but it was shown that the introduction of nonlocality in the imaginary part was still necessary in order to accurately account for particle number and the charge density [22]. Theoretical work provided further support for this introduction of a nonlocal representation of the imaginary part of the self-energy [39, 40]. A review detailing these developments was published in Ref. [23].

2.2.1 Functional form of DOM self-energy

We employ a nonlocal representation of the self-energy following Ref. [22] where $\Sigma_{HF}(\boldsymbol{r},\boldsymbol{r}')$ and $\mathrm{Im}\,\Sigma(\boldsymbol{r},\boldsymbol{r}';E)$ are parametrized and the energy dependence of the real part, $\mathrm{Re}\,\Sigma(\boldsymbol{r},\boldsymbol{r}';E)$, is generated from the dispersion relation in Equation 9. The HF term consists of a volume term, spin-orbit term, and a wine-bottle-shaped term [41],

$$\Sigma_{HF}(\boldsymbol{r},\boldsymbol{r}') = V_{\mathrm{vol}}(\boldsymbol{r},\boldsymbol{r}') + V_{\mathrm{so}}(\boldsymbol{r},\boldsymbol{r}') + V_{\mathrm{wb}}(\boldsymbol{r},\boldsymbol{r}') + \delta(\boldsymbol{r}-\boldsymbol{r}')V_C(r), \tag{10}$$

where the Coulomb potential, $V_C(r)$, is also included. The radial part of our potentials takes the following form,

$$V_{\mathrm{vol}}(\boldsymbol{r},\boldsymbol{r}') = V^{\mathrm{vol}}\quad f\left(\tilde{r},r^{\mathrm{HF}}_{(p,n)},a^{\mathrm{HF}}\right)H\left(\boldsymbol{s};\beta^{\mathrm{HF}}\right), \tag{11}$$

where V^{vol} is a parameter that determines the depth of the potential, and $r^{\mathrm{HF}}_{(p,n)}$, a^{HF}, and β^{HF} are parameters that control the shape of the Woods-Saxon form factor f and Perey–Buck-shaped [34] nonlocality H,

$$\begin{aligned}f(r,r_i,a_i) = \left[1+\exp\left(\frac{r-r_iA^{1/3}}{a_i}\right)\right]^{-1} \\ H(\boldsymbol{s};\beta) = \exp\left(-\boldsymbol{s}^2/\beta^2\right)/\left(\pi^{3/2}\beta^3\right),\end{aligned} \tag{12}$$

and

$$\tilde{r} = \frac{r+r'}{2}\qquad \boldsymbol{s} = \boldsymbol{r}-\boldsymbol{r}'. \tag{13}$$

Nonlocality is introduced in a similar way for $V_{\mathrm{wb}}(\boldsymbol{r},\boldsymbol{r}')$ and $V_{\mathrm{so}}(\boldsymbol{r},\boldsymbol{r}')$; their explicit forms are similar to those in Equations 10–13 and can be found in Ref. [30]. The imaginary self-energy consists of volume, surface, and spin-orbit terms,

$$\begin{aligned}\mathrm{Im}\Sigma(\boldsymbol{r},\boldsymbol{r}';E) = -W^{vol}_{0\pm}(E)f(\tilde{r};r^{vol}_{\pm};a^{vol}_{\pm})H\left(\boldsymbol{s};\beta^{vol}\right) \\ +4\,a^{sur}_{\pm}W^{sur}_{\pm}(E)H(\boldsymbol{s};\beta^{sur})\frac{d}{d\tilde{r}}f(\tilde{r},r^{sur}_{\pm},a^{sur}_{\pm}) \\ +\mathrm{Im}\Sigma_{so}(\boldsymbol{r},\boldsymbol{r}';E),\end{aligned} \tag{14}$$

where $W^{vol}_{0\pm}(E)$ and $W^{sur}_{\pm}(E)$ are energy-dependent depths of the volume and surface potentials, respectively, and the ± subscript indicates there are different forms used above and below the Fermi energy (see Ref. [30] for exact forms). When considering asymmetric nuclei, such as ^{48}Ca and ^{208}Pb, additional terms proportional to the asymmetry, $\alpha_{\mathrm{asy}}=\frac{N-Z}{A}$, are added to $\Sigma_{\mathrm{HF}}(\boldsymbol{r},\boldsymbol{r}')$ and $\mathrm{Im}\Sigma(\boldsymbol{r},\boldsymbol{r}';E)$ for a Lane-like representation [42]. These asymmetric terms introduce additional parameters describing both their radial shape and energy-dependent depths [30] (see Refs. [30, 32] for the full list of parameters used in ^{48}Ca and ^{208}Pb).

As mentioned previously, it was customary in the past to replace nonlocal potentials by local, energy-dependent potentials [21, 24, 34, 43]. The introduction of an energy dependence alters the dispersive correction from Equation (9) and distorts the normalization, leading to incorrect spectral functions and related quantities [38]. Thus, a nonlocal implementation permits the self-energy to accurately reproduce important observables such as charge density, particle number, and ground-state binding energy.

2.3 DOM fits of ^{208}Pb and ^{48}Ca

To use the DOM self-energy for predictions, the parameters of the self-energy are constrained through weighted χ^2 minimization (using the Powell method [44]) by measurements of elastic differential cross sections ($\frac{d\sigma}{d\Omega}$), analyzing powers (A_θ), reaction cross sections (σ_{react}), total cross sections (σ_{tot}), charge density (ρ_{ch}), energy levels ($\varepsilon_{n\ell j}$), particle number, and the root-mean-square charge radius (R_{ch}). The angular dependence of $\Sigma(\boldsymbol{r},\boldsymbol{r}';E)$ is represented in a partial-wave basis, and the radial component is represented in a Lagrange basis using Legendre and Laguerre polynomials for scattering and bound states, respectively. The bound states are found by diagonalizing the Hamiltonian in Equation 6 and the propagator is found by inverting the Dyson equation, Equation 2, whereas all scattering calculations are performed in the framework of R-matrix theory [26]. Whereas it has been suggested in Refs. [45–47] that charge-exchange reactions to isobaric analog states could further constrain the isovector potential, charge-exchange data were not included in the fits reviewed in this

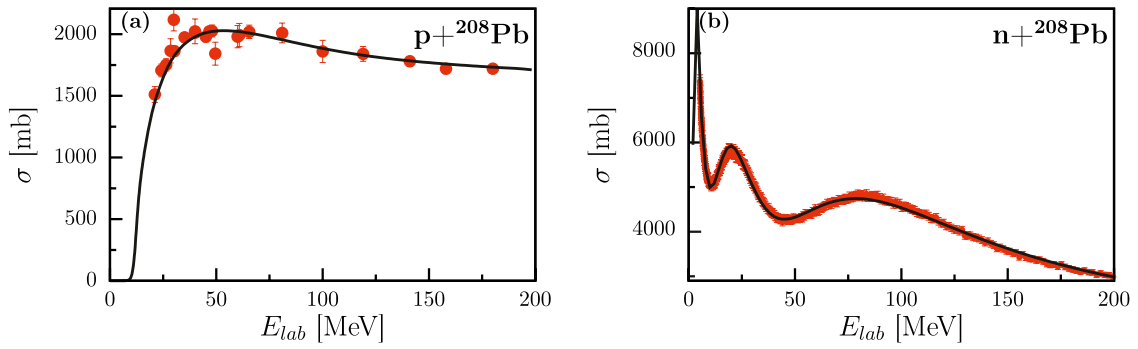

FIGURE 2
(A) Proton reaction cross section in ^{208}Pb. The solid line is generated from the DOM self-energy, whereas the filled circles are from the experiment. **(B)** Neutron total cross section in ^{208}Pb. The solid line is generated from the DOM self-energy for ^{208}Pb, whereas the filled circles are from the experiment (see Ref. [37] for the experimental data. Figure adapted from Ref. [30]).

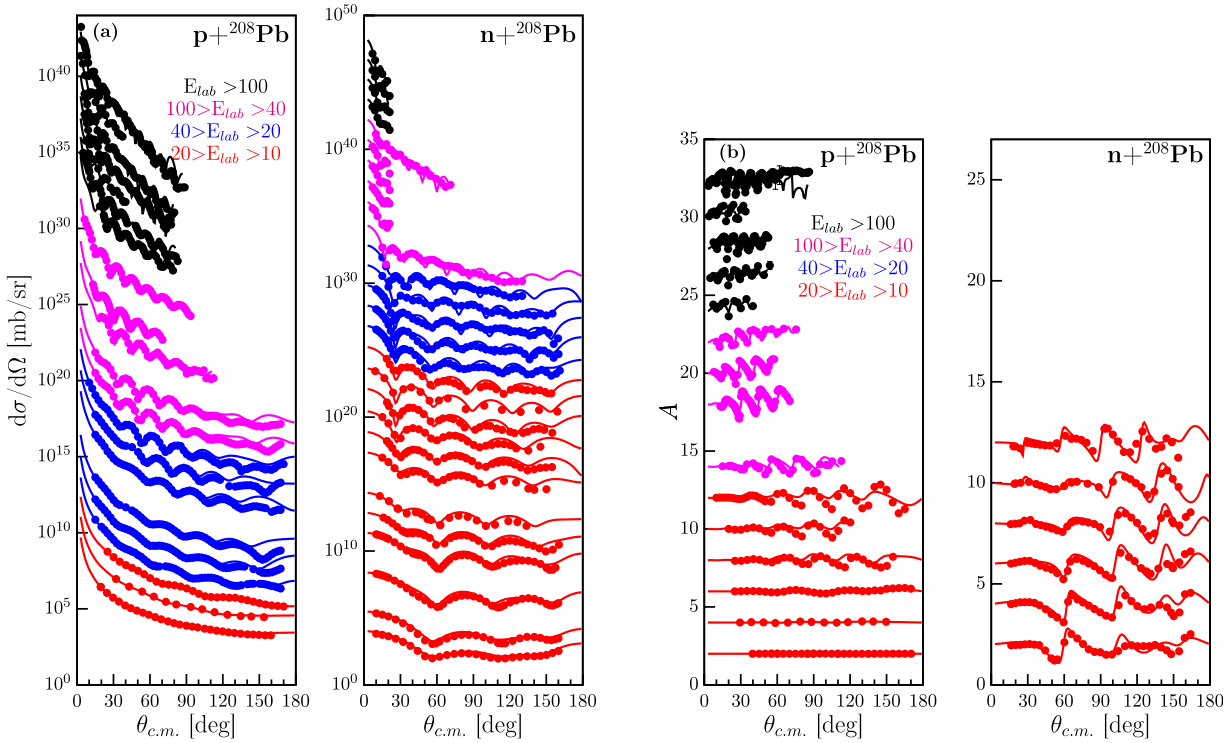

FIGURE 3
(A) Calculated and experimental proton and neutron elastic-scattering angular distributions of the differential cross section $\frac{d\sigma}{d\Omega}$ for ^{208}Pb ranging from 10 MeV to 200 MeV. The data at each energy are offset by factors of ten to help visualize all of the data at once. **(B)** Results for proton and neutron analyzing power generated from the DOM self-energy for ^{208}Pb compared with experimental data ranging from 10 MeV to 200 MeV. References to the data are given in Ref. [37]. Figure adapted from Ref. [30].

article. Reasonable cross sections are obtained with our DOM potential, suggesting that these data, although important, are not sufficient to alter the conclusions of our work significantly. This may be due to the use of nonlocal potentials as opposed to the local ones used in Refs. [45, 46] based on Ref. [48].

When constraining the ^{48}Ca self-energy, the isoscalar part is largely determined by the nearby $N = Z$ ^{48}Ca nucleus. Therefore, using our ^{40}Ca parametrization from Ref. [31] as a starting point, we only needed to fit the asymmetric parameters of the ^{48}Ca potential [25, 30]. This resulted in a ^{48}Ca self-energy that closely reproduced all training data [25]. In the case of ^{208}Pb, there is not a nearby nucleus with $N = Z$; therefore, we started from the ^{48}Ca parameters of Ref. [32] and varied both the isoscalar and isovector parameters to reproduce experimental data. To illustrate how well this method works, we show the result of the ^{208}Pb fit below.

Proton reaction cross sections together with the DOM result are displayed in panel (a) of Figure 2. The neutron total cross section is shown in panel (b) of Figure 2. Both aggregate cross sections play an

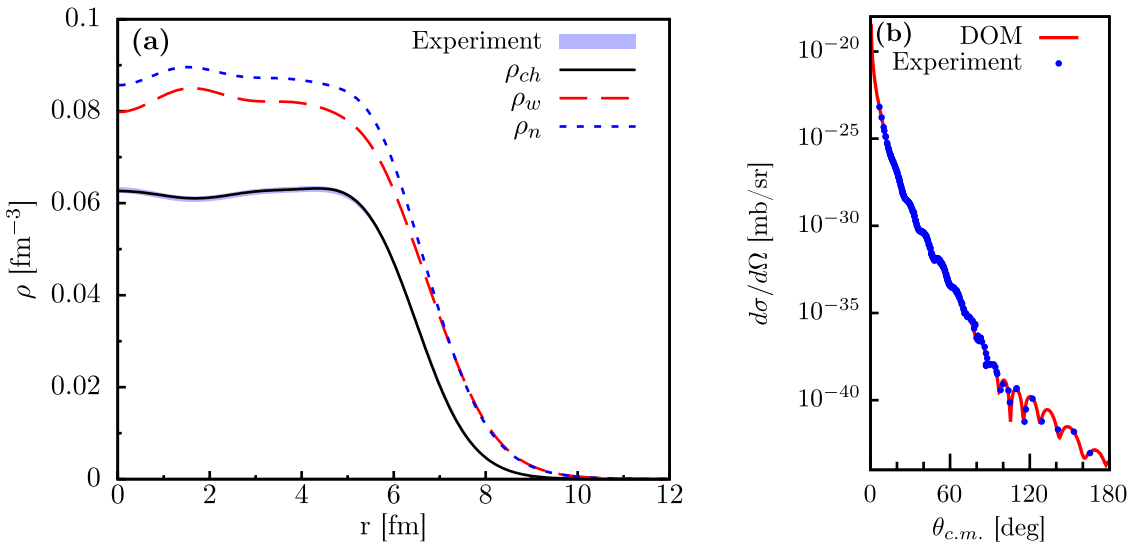

FIGURE 4
(A) Experimental and fitted ^{208}Pb charge density. The solid black line is calculated using Equation 4 and folding with the proton charge distribution, whereas the experimental band represents the 1% error associated with the extracted charge density from elastic electron scattering experiments using the sum of Gaussians parametrization [49, 50]. Also shown is the deduced weak charge distribution, ρ_w (red long-dashed line), and neutron matter distribution, ρ_n (blue short-dashed line). **(B)** Experimental and fitted elastic electron scattering differential cross section in ^{208}Pb. All available data have been transformed to an electron energy of 502 MeV in the center-of-mass frame [51]. Figure adapted from Ref. [30].

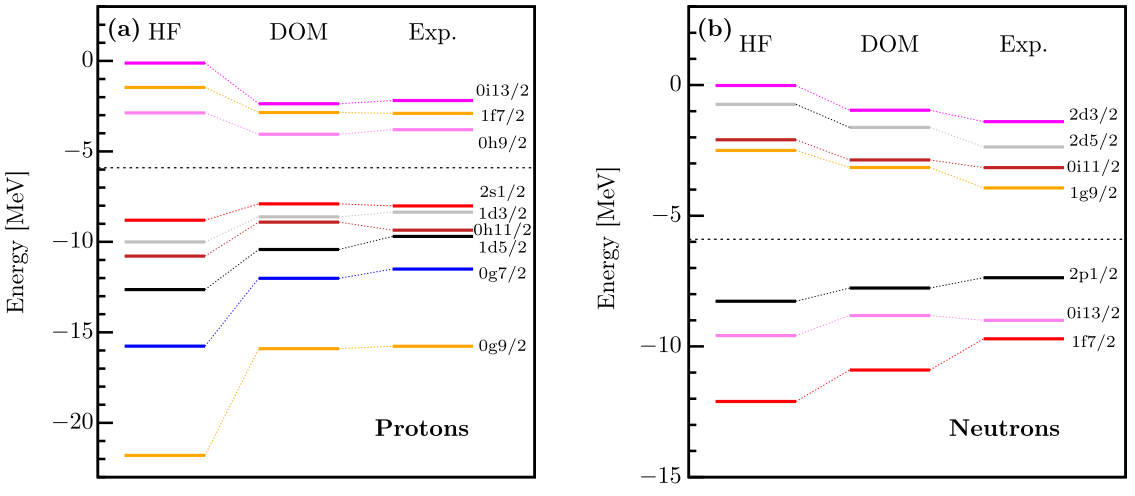

FIGURE 5
(A) Proton and **(B)** neutron energy levels in ^{208}Pb. The energies on the left are calculated using only the static part of the DOM self-energy, corresponding to a Hartree–Fock calculation. The middle energies are those calculated using the full DOM self-energy. The energies on the right correspond to the experimental values. The change from the left energies to the middle energies is the result of including the dynamic part of the self-energy. Figure adapted from Ref. [30].

important role in determining volume integrals of the imaginary part of the self-energy, thereby providing strong constraints on the depletion of IPM orbits. The elastic differential cross sections of proton and neutrons up to 200 MeV are shown in panel (a) of Figure 3. Panel (b) contains the analyzing powers for neutrons and protons which strongly constrain the spin-orbit components of the self-energy.

The charge density of ^{208}Pb is shown in panel (a) of Figure 4. The experimental band is extracted from elastic electron scattering differential cross sections [49]. This dataset is well reproduced after using the DOM charge density from Figure 4 as the ingredient in a relativistic elastic electron scattering code [52]. The corresponding elastic electron scattering cross section is shown in panel (b) of Figure 4 and compared to experiment with all available data transformed to electron energy of 502 MeV in the center-of-mass frame [51].

In Figure 5, single-particle levels calculated using Equation 6 are compared to the experimental values for protons and neutrons in

TABLE 1 Comparison of the calculated DOM particle numbers and binding energy of ^{208}Pb and the corresponding experimental values. The experimental binding energy was taken from Ref. [54]. The experimental charge radius is from Ref. [49].

	N	Z	E_0^A/A [MeV]	R_{ch} [fm]
DOM	126.2	82.08	−7.82	5.48
Expt	126	82	−7.87	5.50

panels (a) and (b), respectively. The middle column consists of levels calculated using the full DOM and the right column contains the experimental levels. The first column of the figures represents a calculation using only the static part of the self-energy, corresponding to the Hartree–Fock (mean-field) contribution. It is clear from these level diagrams that the mean-field overestimates the particle-hole gap (see also Ref. [53]). The inclusion of the dynamic part of the self-energy is necessary to reduce this gap and properly describe the energy levels [21]. Furthermore, the effect of including the dynamic part of the self-energy on the proton levels is stronger than the effect on the neutron levels. This suggests that protons deviate more from the IPM than neutrons in ^{208}Pb.

The number of neutrons and protons in the DOM fit of ^{208}Pb, calculated by integrating Equation 4 using shells up to $\ell \leq 20$, is shown in Table 1. As there are 82 protons and 126 neutrons in ^{208}Pb, the reported values are accurate to within a fraction of a percent. The binding energy of ^{208}Pb was fit to the experimental value using Equation 5. As there is no way at present to assess the contribution of three-body interactions to the ground-state energy, we employ the present approximation which applies when only two-body interactions occur in the Hamiltonian, to ensure that enough spectral strength occurs at negative energy which has implications for the presence of high-momentum components. Also shown in Table 1 is R_{ch}^{208} calculated as the RMS radius of the charge density displayed in Figure 4.

The reproduction of all available experimental data indicates that we have realistic self-energies of ^{208}Pb and similarly for ^{48}Ca [25, 32] capable of describing both bound-state and scattering processes. With these self-energies, we can therefore make predictions of observables such as the neutron skin. Additionally, a parallel DOM analysis of these and other nuclei was conducted using Markov Chain Monte Carlo (MCMC) to optimize the potential parameters employing the same experimental data and a very similar functional form but with a reduced number of parameters. All observables from this MCMC fit fell within one standard deviation of those presented above [55, 56].

2.4 DOM predictions

Spectroscopic factors come directly from the self-energy through Equation 8, making the DOM ideal for predicting $(e,e'p)$ cross sections (see the ^{40}Ca$(e,e'p)^{39}$K analysis in Ref. [31]). When we tried to calculate ^{48}Ca$(e,e'p)^{47}$K using the fit from Ref. [25], we found that the spectroscopic factors were too large to describe the data. Unlike in ^{40}Ca, there is a lack of high-energy ($E > 100$ MeV) proton reaction cross-sectional data in ^{48}Ca. This allowed the fit of Ref. [25] to predict proton reaction cross sections which fell off for higher energies. Consequentially, the ^{48}Ca proton spectroscopic factors were too large to describe ^{48}Ca$(e,e'p)^{47}$K data to the same degree of accuracy achieved for ^{40}Ca [31]. Observing for $E_{\mathrm{c.m.}} > 150$ MeV that $\sigma_{\mathrm{react}}(E)$ is close to constant, we used the ratio of $\sigma_{\mathrm{react}}(E)$ measurements of ^{40}Ca and ^{48}Ca at 700 MeV [57] to scale the ^{40}Ca $\sigma_{\mathrm{react}}(E)$ data such that it could be used as a constraint for ^{48}Ca. Thanks to the dispersion relation, Equation 9, the increased $\mathrm{Im}\Sigma(r,r';E)$ to accommodate higher reaction cross sections at positive energies pulls strength from below ε_F. This reduced the spectroscopic factors which then allowed for accurate descriptions of ^{48}Ca$(e,e'p)^{47}$K cross sections [32]. This only altered the proton parameters; thus, the neutron skin remained unchanged at $R_{\mathrm{skin}} = 0.25$ fm. This demonstrates that once a sufficiently complete set of data is used, the DOM is capable of making accurate predictions.

The valence spectroscopic factors in ^{208}Pb are consistent with the observations of Ref. [58] and the interpretation of Ref. [59]. The past extraction of spectroscopic factors using the $(e,e'p)$ reaction yielded a value around 0.65 for the valence 2s1/2 orbit [60] based on the results of Refs. [61, 62]. Although the use of nonlocal optical potentials may slightly increase this value as shown in Ref. [31], it may be concluded that the value of 0.69 obtained from the DOM analysis is consistent with the past result. Nikhef data obtained in a large missing energy and momentum domain [63] can now be consistently analyzed employing the complete DOM spectral functions.

Correlations can also be studied through the momentum distribution, $n(k)$, which represents the diagonal of the double Fourier transform of the single-particle density matrix. The calculated DOM momentum distributions of ^{48}Ca and ^{208}Pb are shown in Figure 6. The high-momentum tail of $n(k)$ arises from short-range correlations (SRCs), which is another manifestation of many-body correlations beyond the IPM description of the nucleus [64]. This high-momentum content can be quantified by integrating the momentum distribution above the Fermi momentum. Using $k_F = 270$ MeV/c, 13.4% of protons and 10.7% of neutrons have momenta greater than k_F in ^{208}Pb, whereas ^{48}Ca has 14.6% high-k protons and 12.6% high-k neutrons. These numbers are in qualitative agreement with what is observed in the high-momentum knockout experiments conducted by the CLAS collaboration at Jefferson Lab [65]. Furthermore, the fraction of high-momentum protons is larger than the fraction of high-momentum neutrons. These features were predicted by *ab initio* calculations of asymmetric nuclear matter reported in Refs. [66–68] which demonstrated unambiguously that the inclusion of the nucleon–nucleon tensor force, when constrained by nucleon–nucleon scattering data, is responsible for making protons more correlated with increasing nucleon asymmetry at normal density. This supports the np-dominance picture in which the dominant contribution to SRC pairs comes from np SRC pairs which arise from the tensor force in the nucleon–nucleon interaction [69, 70]. Due to the neutron excess in ^{208}Pb and ^{48}Ca, there are more neutrons available to make np SRC pairs which lead to an increase in the fraction of high-momentum protons.

In the DOM, this high-momentum content is determined by how much strength exists in the hole spectral function at large, negative energies. The hole spectral function is constrained in the fit by the particle number, binding energy, and charge density. Whereas the particle number and charge density can only constrain the total strength of the hole spectral function, the binding energy constrains

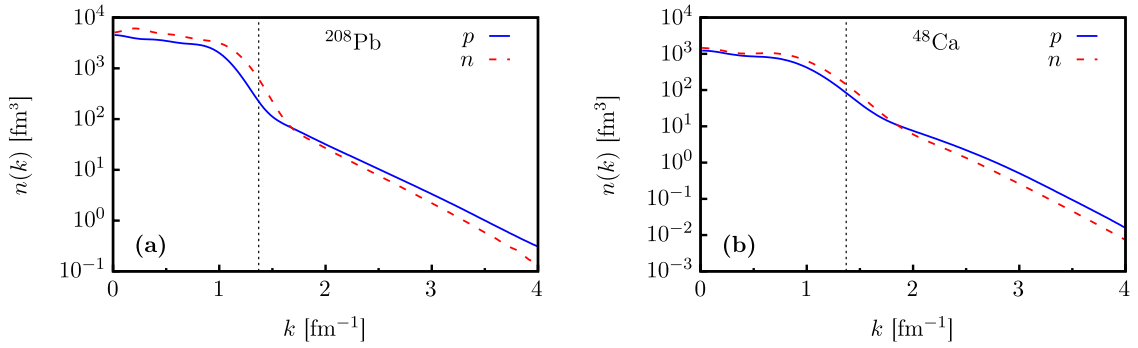

FIGURE 6
Comparison of calculated DOM momentum distributions of protons (solid blue line) and neutrons (dashed red line). The vertical dotted line marks the location of k_F. **(A)** Momentum distributions in ^{208}Pb. **(B)** Momentum distributions in ^{48}Ca. Figure adapted from Refs. [30, 32].

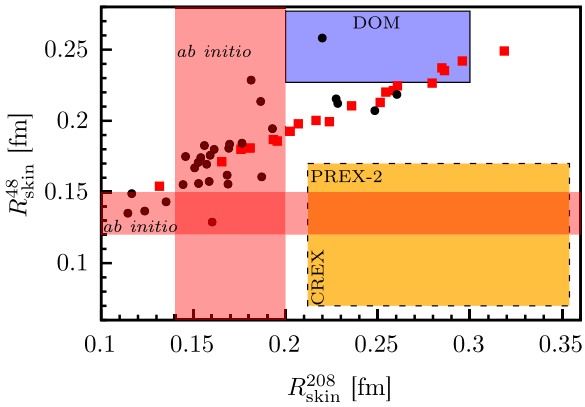

FIGURE 7
Dashed rectangle represents the CREX and PREX-2 analysis [73, 74]. The shaded rectangle labeled DOM represents the DOM results for ^{208}Pb and ^{48}Ca [25, 30]. Smaller squares and circles refer to relativistic and non-relativistic mean-field calculations, respectively, cited in Ref. [72]. The *ab initio* predictions from Ref. [17] for ^{48}Ca and Refs. [18, 19] for ^{208}Pb are represented by horizontal and vertical bands labeled *ab initio*, respectively. All uncertainties are reported at the 1σ level. Figure adapted from Refs. [30, 72].

how the strength of the spectral function is distributed in energy. This arises from the energy-weighted integral in Equation 5, which will push strength of the spectral function to more negative energies in order to achieve more binding. This, in turn, alters the momentum distribution, thus partially constraining the high-momentum content. It should be noted that the DOM does not exhibit the characteristic energy dependence of high-momentum strength distributions [71] as reported in Ref. [22]. Such a dependence is more difficult to be implemented as it requires abandoning the factorization of spatial and energy dependence of the DOM self-energy (see Equation 14).

3 Neutron skin

As demonstrated in the previous section, our constrained self-energies for ^{48}Ca and ^{208}Pb utilize both scattering and bound-state data for a robust picture of nuclei. These fits resulted in thick skins in both ^{48}Ca, $R^{\rm DOM48}_{\rm skin} = 0.25 \pm 0.023$ fm, and ^{208}Pb, $R^{\rm DOM208}_{\rm skin} = 0.25 \pm 0.05$ fm using the uncertainty quantification clarified in Refs. [25, 30]. These results are represented by the shaded box labeled DOM in Figure 7 which is north of the overlapping regions of CREX and PREX-2 (see dashed rectangle). Also included in Figure 7 is the coupled-cluster result for ^{48}Ca from Ref. [17] as a horizontal band, the *ab initio* results for ^{208}Pb reported in Refs. [18, 19] as a vertical band, and both relativistic and non-relativistic mean-field calculations represented by squares and circles, respectively [72].

At the time of our calculations, CREX had not been reported and only the first PREX experiment with large uncertainty had been reported, meaning that there was not an easy metric to gauge the accuracy of our predictions. Therefore, we took advantage of the unique characteristic of the DOM to explore which measurements, in either the bound or scattering domains, provide signatures of the neutron skin. To accomplish this, additional ^{48}Ca fits were performed in which selected values of R_n are forced (i.e., heavily weighted) in the corresponding χ^2 minimization [23]. This is achieved by varying the radius parameters of the main real potential (r_n^{HF} and r_n^{HFasy} [25]) and refitting the other asymmetry-dependent parameters. The weighted χ^2 as a function of the calculated R_n is plotted as the points (traced by the solid black line) in Figure 8C and the absolute minimum at $R_n = 3.67$ fm corresponds to the skin thickness of $R_{\rm skin} = 0.25$ fm. There is some fine-scale jitter in the variation of χ^2 with R_n. To concentrate on the larger-scale variation, the data points shown in Figure 8C are local averages with the error bars giving the range of the jitter.

The location of the *ab initio* coupled-cluster result [17] is also indicated at R_n ~3.56 fm as a blue square. The shown χ^2 has been subdivided into its contributions from its two most important components (dashed curves): the elastic-scattering angular distributions and the total neutron cross sections. The former has a smaller sensitivity to R_n, and its χ^2 is slightly lower for the smaller values of R_n, which are more consistent with the *ab initio* and CREX results as illustrated in Figure 8A where a fit with a forced value of $R_{\rm skin} = 0.132$ is compared to the best DOM fit and to the data. Whereas this alternative calculation improves the reproduction of these data, the deviations of both curves from the data are typical of what one sees in global optical-model fits. In addition, the available

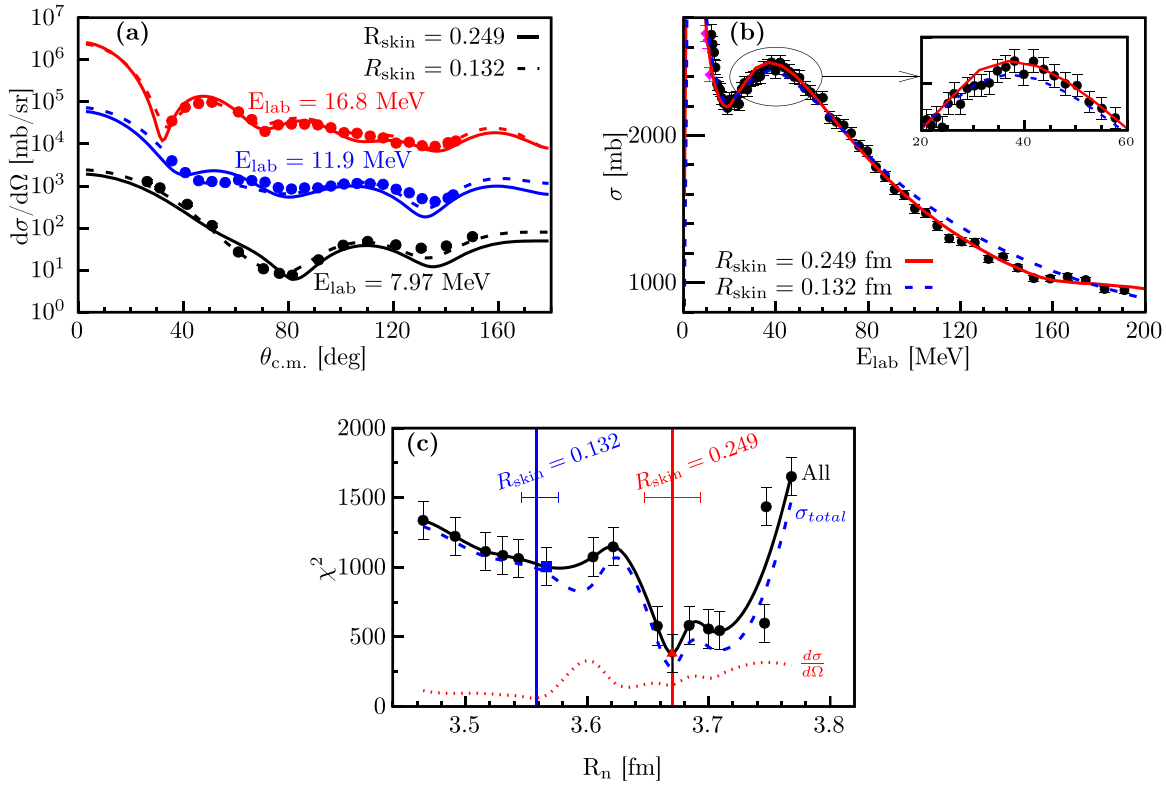

FIGURE 8
(A) Comparison of experimental n+^{48}Ca elastic-scattering angular distributions [37, 75] to the best DOM fit of all data (solid curves) and to a constrained fit with the skin thickness forced to R_{skin} = 0.132 fm (dashed curves) consistent with the *ab initio* and CREX values. **(B)** Comparison of the experimental total neutron cross sections of ^{48}Ca (diamonds [76], circles [77]) to DOM fits with constrained values of R_n. **(C)** χ^2 from fitting all data (solid curve) and its contribution from fitting the elastic-scattering angular distributions and total neutron cross section (dotted and dashed curves, respectively). Each point corresponds to a fit around its value of R_n. Figure adapted from Ref. [25].

experimental angular distributions only cover a small range of bombarding energies (7.97–16.8 MeV) and may not be typical of other energies.

The total cross section exhibits larger sensitivity and the experimental data cover a large range of neutron energies (6–200 MeV). Two datasets are available (circles and diamonds in Figure 8B) but are inconsistent by ~10% at E_{lab} ~10 MeV, where their ranges overlap. The high-energy dataset [77] (circles) was used in the DOM fit as it was obtained with ^{48}Ca metal, whereas the low-energy set [76] (diamonds) employed $^{48}CaCO_3$ and required a subtraction of ~70% of the signal due to neutron absorption from the CO_3 component. Therefore, the χ^2 contribution is displayed only from the high-energy set. This χ^2 exhibits a broad minimum from R_n = 3.66 to 3.75 fm, allowing values of R_{skin} up to 0.33 fm.

It appeared that the total cross section provided a strong constraint on the neutron skin (as an example of a scattering observable that can affect bound-state observables through the dispersion relation). Faced with the thin skin reported by CREX, it appears that we did not attribute enough uncertainty in the total cross-sectional data to allow a wider range of skin values. This concept will be explored in future DOM investigations of R^{48}_{skin} in which the CREX measurement is included in the fit. It is possible that increasing the uncertainty in the high-energy σ_{tot} data would allow for skin values consistent with CREX (i.e., the blue square in Figure 8C) to have χ^2 values comparable to those of the current DOM fit. Furthermore, similar to the analysis that resulted in Figure 8, it will be interesting to see how the CREX constraint alters other aspects of the DOM self-energy, even non-observables features such as the shape of the spectral functions (see Figure 1) and the momentum distributions (see Figure 6).

Provided with a sufficiently complete set of data, which is the case for protons in ^{48}Ca, the DOM framework allows for accurate predictions (see Sec. 2.4). The thin skin of CREX demonstrates that, unlike protons, there are not sufficient experimental data for neutrons in ^{48}Ca to accurately predict the neutron skin. The number of proton elastic-scattering datasets at different energies shown for ^{208}Pb in Figure 3 is representative of p+^{48}Ca, whereas the three datasets in Figure 8A display all available data for n+^{48}Ca elastic-scattering. Furthermore, there are only neutron total cross-sectional data, and no reaction cross-sectional data exist at any energy in ^{48}Ca. Thus, even at positive energies, the DOM neutrons are not constrained nearly as well as protons. With more neutron scattering data in ^{48}Ca, the DOM could provide a better prediction of R^{48}_{skin}. Furthermore, the inclusion of the CREX data point will provide a much needed constraint below the Fermi energy, bringing the neutron dataset closer to "completeness" (in the sense of constraining the DOM).

To accommodate the thin skin extracted by CREX, one would expect the distribution of neutrons to favor a configuration with

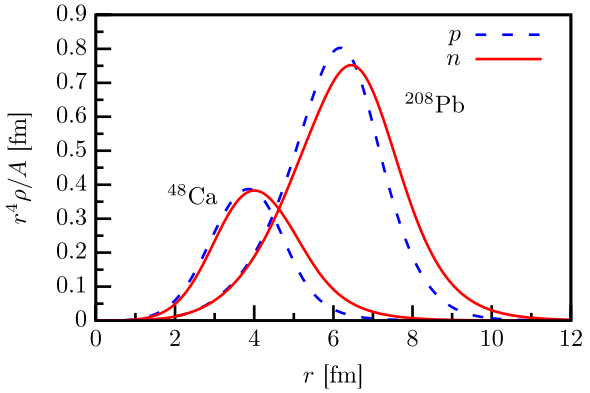

FIGURE 9
Neutron (red solid line) and proton (blue dashed line) point distributions in ^{208}Pb and ^{48}Ca weighted by r^4 while normalized to particle number. Figure adapted from Ref. [30].

TABLE 2 DOM predicted neutron skins for ^{40}Ca,^{48}Ca, and^{208}Pb. Also shown are the neutron skins normalized by R_p, denoted as $\tilde{R}_{\rm skin}$, as well as neutron skins with the Coulomb potential removed from the self-energy, denoted as $R^{noC}_{\rm skin}$. The last entry is the normalized neutron skin with Coulomb removed, $\tilde{R}^{noC}_{\rm skin}$.

Nucleus	^{40}Ca	^{48}Ca	^{208}Pb
α_{asy}	0	0.167	0.211
R_p	3.39 fm	3.38 fm	5.45 fm
R_n	3.33 fm	3.63 ± 0.023 fm	5.70 ± 0.05 fm
$R_{\rm skin}$	−0.06 fm	0.25 ± 0.023 fm	0.25 ± 0.05 fm
$\tilde{R}_{\rm skin}$	−0.017	0.070 ± 0.0067	0.046 ± 0.0092
$R^{noC}_{\rm skin}$	0 fm	0.309 ± 0.023 fm	0.380 ± 0.05 fm
$\tilde{R}^{noC}_{\rm skin}$	0	0.089 ± 0.0067	0.070 ± 0.0092

more neutrons in the interior of ^{48}Ca. This concentration of neutrons near the origin implies an increase in the fraction of high-momentum neutrons, thanks to the Heisenberg uncertainty principle. This could lead to a larger percentage of high-momentum neutrons than protons, which would be a departure from the current DOM picture (see Figure 6) as well as from the evidence suggested by the CLAS experiments on other asymmetric nuclei. It could turn out that the size of ^{48}Ca is inadequate to apply bulk nuclear properties to. We observed this in Ref. [28], where we consider the interiors of ^{48}Ca and ^{208}Pb as representing saturated nuclear matter. We found that the smaller size of ^{48}Ca than that of ^{208}Pb is harder to connect with saturated nuclear matter.

The neutron and proton point distributions in ^{208}Pb and ^{48}Ca, weighted by r^4 and normalized by particle number, are shown in Figure 9 The difference between proton and neutron distributions is highlighted by the r^4 factor which is employed when integrating the particle distributions to calculate the RMS radii. The DOM predictions of the neutron skin of ^{40}Ca, ^{48}Ca, and ^{208}Pb are shown in Table 2, where it is evident that the DOM neutron skins of ^{48}Ca and ^{208}Pb are very similar. As ^{208}Pb and ^{48}Ca are similar $\alpha_{\rm asy}$ (see Table 2), it may seem reasonable that they have similar neutron skins. However, the particle distributions of ^{208}Pb and ^{48}Ca in Figure 9, even though normalized by particle number, are quite distinct due to the size difference of the nuclei. In light of this, the neutron skin of ^{208}Pb is biased to be larger by the increase in the RMS radii of the proton and neutron distributions. Thus, an interesting comparison can be made by normalizing $R_{\rm skin}$ by R_p,

$$\tilde{R}_{\rm skin} = \frac{1}{R_p} R_{\rm skin} = \frac{R_n}{R_p} - 1, \tag{15}$$

where $\tilde{R}_{\rm skin}$ is the normalized neutron skin thickness. This normalization serves to remove size dependence when comparing neutron skins of different nuclei. The result of the normalization in Equation 15 is shown in Table 2. The difference between the normalized skins of ^{208}Pb and ^{48}Ca in Table 2 reveals that the RMS radius of the neutron distribution does not simply scale by the size of the nucleus for nuclei with similar asymmetries. Although it is true that the nuclear charge radius scales roughly by $A^{1/3}$ (and by extension so does R_p), the same cannot be said about R_n.

If one is to scale by the size of the nucleus, then the extension of the proton distribution due to Coulomb repulsion (which scales with the number of protons) should also be considered. As ^{208}Pb has four times as many protons as ^{48}Ca, the effect of Coulomb repulsion on the neutron skin of ^{208}Pb could be up to four times more than its effect on the ^{48}Ca neutron skin, which can reasonably be taken from the predicted skin of −0.06 fm in ^{40}Ca. In order to further investigate the effects of the Coulomb force on the neutron skin, we removed the Coulomb potential from the DOM self-energy. In doing this, the quasihole energy levels become much more bound, which increases the number of protons. To account for this, we shifted ε_F such that it remains between the particle-hole gap of the protons in ^{208}Pb, corresponding to a shift of 19 MeV. Removing the effects of the Coulomb potential leads to an increased neutron skin of 0.38 fm. The results of the normalized neutron skins with Coulomb removed are listed in Table 2 for each nucleus, where it is clear that the Coulomb potential has a strong effect on the neutron skin. This points to the fact that the formation of a neutron skin cannot be explained by the asymmetry alone. Whereas the asymmetry in ^{48}Ca is primarily caused by the additional neutrons in the f7/2 shell, there are several different additional shell fillings between the neutrons and protons in ^{208}Pb. It is evident that these shell effects make it more difficult to predict the formation of the neutron skin based on macroscopic properties alone.

4 Conclusion

We have reviewed a nonlocal dispersive optical-model analysis of ^{48}Ca and ^{208}Pb in which we fit elastic-scattering angular distributions, absorption and total cross sections, single-particle energies, charge densities, ground-state binding energies, and particle numbers. When sufficient data are available to constrain our self-energies, the DOM is capable of accurate predictions. With our well-constrained self-energies, we report non-negligible high-momentum content in both ^{48}Ca and ^{208}Pb, which is consistent with the experimental observations at JLAB [64, 65, 69]. Spectroscopic factors are automatically generated and reproduce ^{48}Ca$(e,e'p)^{47}$K experimental momentum distributions

and those predicted in ^{208}Pb appear consistent with the most up-to-date analysis of the $(e, e'p)$ reaction for the last valence proton orbit [60]. Furthermore, these spectroscopic factors explain the reduction of the form factors of high spin states obtained in inelastic electron scattering [58], lending support to the interpretation of Ref. [59]. The thick skin predicted in ^{208}Pb ($R^{208}_{\text{skin}} = 0.25 \pm 0.05$) is in agreement with PREX-2, whereas that predicted in ^{48}Ca ($R^{48}_{\text{skin}} = 0.25 \pm 0.023$) is not consistent with CREX. With more neutron scattering data in ^{48}Ca, the DOM could provide a better prediction of R^{48}_{skin}. Including the CREX result in a DOM fit of ^{48}Ca would provide a much needed constraint, bringing the neutron dataset closer to "completeness."

To reproduce the reduced neutron RMS radius reported by CREX, we expect that the neutron distribution in ^{48}Ca would shrink such that more neutrons concentrate in the interior of ^{48}Ca. This redistribution would translate to increased high-momentum neutrons which could invert the hierarchy of the current DOM fit in which there is a higher percentage of high-momentum protons than neutrons (see Figure 6), counter to the evidence suggested by the CLAS experiments on other asymmetric nuclei [65, 69]. Currently, this is speculation, but we are exploring new DOM fits using CREX as an additional constraint so we can reach a better understanding. We must also consider the possibility that the size of ^{48}Ca is inadequate for extracting/applying bulk nuclear properties. The shell-closure of the $f7/2$ neutrons in ^{48}Ca, for example, could be playing a stronger role in the formation of the skin than the EOS. Similarly, it is possible that this np dominance picture is distorted by finite-nucleus effects that are not negligible in ^{48}Ca. The DOM provides a unique perspective of the nucleus in that we can link these entirely different measurements through the dispersion relation in order to reach a deeper understanding of the relation between the EOS (and hence exotic objects such as neutron stars) and finite nuclei.

The DOM analysis provides an alternative approach to the multitude of mean-field calculations that provide a large variety of results for the neutron skins of ^{48}Ca and ^{208}Pb [72] while also contrasting with the *ab initio* result of Ref. [17] for ^{48}Ca and Refs. [18, 19] for ^{208}Pb. The experiments employing parity-violating elastic electron scattering on these nuclei [14, 15] therefore remain the most unambiguous approach to determine the neutron skin. A systematic study of more nuclei with similar asymmetry, α_{asy}, to ^{208}Pb and ^{48}Ca would help in determining the details of the formation of the neutron skin. This will lead to a better understanding of the EOS, which is vital in the current multi-messenger era onset by the first direct detection of a neutron star merger [78].

Author contributions

MA: conceptualization, data curation, formal analysis, funding acquisition, investigation, methodology, project administration, resources, software, supervision, validation, visualization, writing–original draft, and writing–review and editing. WD: conceptualization, formal analysis, funding acquisition, investigation, methodology, project administration, resources, supervision, validation, writing–original draft, and writing–review and editing.

Funding

The author(s) declare that financial support was received for the research, authorship, and/or publication of this article. This work was performed under the auspices of the U.S. Department of Energy by Lawrence Livermore National Laboratory under Contract DE-AC52-07NA27344 and was supported by the LLNL-LDRD Program under Project No. 24-LW-062. This work was also supported by the U.S. National Science Foundation under grants PHY-1912643 and PHY-2207756.

Acknowledgments

The authors acknowledge the important early contributions to this research from Bob Charity, Hossein Mahzoon, Cole Pruitt, and Lee Sobotka.

Conflict of interest

The authors declare that the research was conducted in the absence of any commercial or financial relationships that could be construed as a potential conflict of interest.

Publisher's note

References

1. Typel S, Brown BA. Neutron radii and the neutron equation of state in relativistic models. *Phys Rev C* (2001) 64:027302. doi:10.1103/PhysRevC.64.027302

2. Furnstahl RJ, Hammer H. *Phys Lett B* (2002) 531:203–8. doi:10.1016/s0370-2693(01)01504-0

3. Steiner A, Prakash M, Lattimer J, Ellis P. Isospin asymmetry in nuclei and neutron stars. *Phys Rep* (2005) 411:325–75. doi:10.1016/j.physrep.2005.02.004

4. Roca-Maza X, Centelles M, Viñas X, Warda M. Neutron skin of ^{208}Pb, nuclear symmetry energy, and the parity radius experiment. *Phys Rev Lett* (2011) 106:252501. doi:10.1103/PhysRevLett.106.252501

5. Horowitz CJ, Piekarewicz J. Neutron star structure and the neutron radius of ^{208}pb. *Phys Rev Lett* (2001) 86:5647–50. doi:10.1103/PhysRevLett.86.5647

6. Steiner AW, Lattimer JM, Brown EF. The equation of state from observed masses and radii of neutron stars. *The Astrophysical J* (2010) 722:33–54. doi:10.1088/0004-637x/722/1/33

7. Li BA, Chen LW, Ko CM. Recent progress and new challenges in isospin physics with heavy-ion reactions. *Phys Rep* (2008) 464:113–281. doi:10.1016/j.physrep.2008.04.005

8. Tsang MB, Stone JR, Camera F, Danielewicz P, Gandolfi S, Hebeler K, et al. Constraints on the symmetry energy and neutron skins from experiments and theory. *Phys Rev C* (2012) 86:015803. doi:10.1103/PhysRevC.86.015803

9. Mammei JM, Horowitz CJ, Piekarewicz J, Reed BT, Sfienti C. Neutron skins: weak elastic scattering and neutron stars. *Annu Rev Nucl Part Sci* (2024) 74:321–42. doi:10.1146/annurev-nucl-102122-024207

10. Angeli I, Marinova K. Table of experimental nuclear ground state charge radii: an update. *At Data Nucl Data Tables* (2013) 99:69–95. doi:10.1016/j.adt.2011.12.006

11. Garcia Ruiz RF, Bissell ML, Blaum K, Ekstrom A, Frommgen N, Hagen G, et al. Unexpectedly large charge radii of neutron-rich calcium isotopes. *Nat Phys*. (2016) 594–8. doi:10.1038/nphys3645

12. Horowitz CJ. Parity violating elastic electron scattering and coulomb distortions. *Phys Rev C* (1998) 57:3430–6. doi:10.1103/PhysRevC.57.3430

13. Abrahamyan S, Ahmed Z, Albataineh H, Aniol K, Armstrong DS, Armstrong W, et al. Measurement of the neutron radius of ^{208}Pb through parity violation in electron scattering. *Phys Rev Lett* (2012) 108:112502. doi:10.1103/PhysRevLett.108.112502

14. Adhikari D, Albataineh H, Androic D, Aniol K, Armstrong D, Averett T, et al. Accurate determination of the neutron skin thickness of ^{208}Pb through parity-violation in electron scattering. *Phys Rev Lett* (2021) 126:172502. doi:10.1103/PhysRevLett.126.172502

15. Adhikari D, Albataineh H, Androic D, Aniol K, Armstrong D, Averett T, et al. Precision determination of the neutral weak form factor of ^{48}Ca. *Phys Rev Lett* (2022) 129:042501. doi:10.1103/PhysRevLett.129.042501

16. Reinhard PG, Roca-Maza X, Nazarewicz W. Combined theoretical analysis of the parity-violating asymmetry for ^{48}Ca and ^{208}Pb. *Phys Rev Lett* (2022) 129:232501. doi:10.1103/PhysRevLett.129.232501

17. Hagen G, Ekström A, Forssén C, Jansen GR, Nazarewicz W, Papenbrock T, et al. Neutron and weak-charge distributions of the 48ca nucleus. *Nat Phys* (2016) 12:186–90. doi:10.1038/nphys3529

18. Hu B, Jiang W, Miyagi T, Sun Z, Ekström A, Forssén C, et al. *Ab initio* predictions link the neutron skin of 208pb to nuclear forces. *Nat Phys* (2022) 18:1196–200. doi:10.1038/s41567-022-01715-8

19. Hu B, Jiang W, Miyagi T, Sun Z, Ekström A, Forssén C, et al. Author correction: *ab initio* predictions link the neutron skin of 208pb to nuclear forces. *Nat Phys* (2024) 20:169. doi:10.1038/s41567-023-02324-9

20. Reed BT, Fattoyev FJ, Horowitz CJ, Piekarewicz J. Density dependence of the symmetry energy in the post–prex-crex era. *Phys Rev C* (2024) 109:035803. doi:10.1103/PhysRevC.109.035803

21. Mahaux C, Sartor R. *Single-particle motion in nuclei*. Boston, MA: Springer US (1991). p. 1–223. doi:10.1007/978-1-4613-9910-0_1

22. Mahzoon MH, Charity RJ, Dickhoff WH, Dussan H, Waldecker SJ. Forging the link between nuclear reactions and nuclear structure. *Phys Rev Lett* (2014) 112:162503. doi:10.1103/PhysRevLett.112.162503

23. Dickhoff WH, Charity RJ, Mahzoon MH. Novel applications of the dispersive optical model. *J Phys G: Nucl Part Phys* (2017) 44:033001. doi:10.1088/1361-6471/44/3/033001

24. Dickhoff WH, Van Neck D. *Many-body theory exposed*. 2nd ed. New Jersey: World Scientific (2008).

25. Mahzoon MH, Atkinson MC, Charity RJ, Dickhoff WH. Neutron skin thickness of Ca48 from a nonlocal dispersive optical-model analysis. *Phys Rev Lett* (2017) 119:222503. doi:10.1103/PhysRevLett.119.222503

26. Descouvemont P, Baye D. The r -matrix theory. *Rep Prog Phys* (2010) 73:036301. doi:10.1088/0034-4885/73/3/036301

27. Atkinson MC. *Developing nucleon self-energies to generate the ingredients for the description of nuclear reactions*. Springer (2020).

28. Atkinson MC, Dickhoff WH, Piarulli M, Rios A, Wiringa RB. Reexamining the relation between the binding energy of finite nuclei and the equation of state of infinite nuclear matter. *Phys Rev C* (2020) 102:044333. doi:10.1103/PhysRevC.102.044333

29. Atkinson MC, Dickhoff WH, Piarulli M, Rios A, Wiringa RB. Reply to "comment on 'reexamining the relation between the binding energy of finite nuclei and the equation of state of infinite nuclear matter' ". *Phys Rev C* (2021) 104:059802. doi:10.1103/PhysRevC.104.059802

30. Atkinson MC, Mahzoon MH, Keim MA, Bordelon BA, Pruitt CD, Charity RJ, et al. Dispersive optical model analysis of ^{208}Pb generating a neutron-skin prediction beyond the mean field. *Phys Rev C* (2020) 101:044303. doi:10.1103/PhysRevC.101.044303

31. Atkinson MC, Blok HP, Lapikás L, Charity RJ, Dickhoff WH. Validity of the distorted-wave impulse-approximation description of Ca40(e,e′p)K39 data using only ingredients from a nonlocal dispersive optical model. *Phys Rev C* (2018) 98:044627. doi:10.1103/PhysRevC.98.044627

32. Atkinson MC, Dickhoff WH. Investigating the link between proton reaction cross sections and the quenching of proton spectroscopic factors in 48ca. *Phys Lett B* (2019) 798:135027. doi:10.1016/j.physletb.2019.135027

33. Bell JS, Squires EJ. A formal optical model. *Phys Rev Lett* (1959) 3:96–7. doi:10.1103/PhysRevLett.3.96

34. Perey F, Buck B. A non-local potential model for the scattering of neutrons by nuclei. *Nucl Phys* (1962) 32:353–80. doi:10.1016/0029-5582(62)90345-0

35. Charity RJ, Sobotka LG, Dickhoff WH. Asymmetry dependence of proton correlations. *Phys Rev Lett* (2006) 97:162503. doi:10.1103/PhysRevLett.97.162503

36. Charity RJ, Mueller JM, Sobotka LG, Dickhoff WH. Dispersive-optical-model analysis of the asymmetry dependence of correlations in ca isotopes. *Phys Rev C* (2007) 76:044314. doi:10.1103/PhysRevC.76.044314

37. Mueller JM, Charity RJ, Shane R, Sobotka LG, Waldecker SJ, Dickhoff WH, et al. Asymmetry dependence of nucleon correlations in spherical nuclei extracted from a dispersive-optical-model analysis. *Phys Rev C* (2011) 83:064605. doi:10.1103/PhysRevC.83.064605

38. Dickhoff WH, Van Neck D, Waldecker SJ, Charity RJ, Sobotka LG. Nonlocal extension of the dispersive optical model to describe data below the fermi energy. *Phys Rev C* (2010) 82:054306. doi:10.1103/PhysRevC.82.054306

39. Waldecker SJ, Barbieri C, Dickhoff WH. Microscopic self-energy calculations and dispersive optical-model potentials. *Phys Rev C* (2011) 84:034616. doi:10.1103/PhysRevC.84.034616

40. Dussan H, Waldecker SJ, Dickhoff WH, Müther H, Polls A. Microscopic self-energy of ^{40}ca from the charge-dependent bonn potential. *Phys Rev C* (2011) 84:044319. doi:10.1103/PhysRevC.84.044319

41. Brida I, Pieper SC, Wiringa RB. Quantum Monte Carlo calculations of spectroscopic overlaps in$A\leqslant 7$nuclei. *Phys Rev C* (2011) 84:024319. doi:10.1103/physrevc.84.024319

42. Lane AM. Isobaric spin dependence of the optical potential and quasi-elastic (p, n) reactions. *Nucl Phys* 35 (1962) 676. doi:10.1016/0029-5582(62)90153-0

43. Fiedeldey H. The equivalent local potential and the perey effect. *Nucl Phys* (1966) 77:149–56. doi:10.1016/0029-5582(66)90682-1

44. Press WH, Teukolsky SA, Vetterling WT, Flannery BP. *Numerical recipes in fortran 90*. Cambridge University Press (1996).

45. Khoa DT, Than HS, Cuong DC. Folding model study of the isobaric analog excitation: isovector density dependence, lane potential, and nuclear symmetry energy. *Phys Rev C* (2007) 76:014603. doi:10.1103/PhysRevC.76.014603

46. Loc BM, Khoa DT, Zegers RGT. Charge-exchange scattering to the isobaric analog state at medium energies as a probe of the neutron skin. *Phys Rev C* (2014) 89:024317. doi:10.1103/PhysRevC.89.024317

47. Danielewicz P, Singh P, Lee J. Symmetry energy III: isovector skins. *Nucl Phys A* (2017) 958:147–86. doi:10.1016/j.nuclphysa.2016.11.008

48. Koning A, Delaroche J. Local and global nucleon optical models from 1 kev to 200 mev. *Nucl Phys A* (2003) 713:231–310. doi:10.1016/S0375-9474(02)01321-0

49. de Vries H, de Jager CW, de Vries C. Nuclear charge-density-distribution parameters from elastic electron scattering. *Nucl Data Tables* (1987) 36:495–536. doi:10.1016/0092-640x(87)90013-1

50. Sick I, Bellicard JB, Cavedon JM, Frois B, Huet M, Leconte P, et al. Charge density of 40Ca. *Phys Lett B* (1979) 88:245–8. doi:10.1016/0370-2693(79)90458-1

51. Frois B, Bellicard JB, Cavedon JM, Huet M, Leconte P, Ludeau P, et al. High-momentum-transfer electron scattering from ^{208}Pb. *Phys Rev Lett* (1977) 38:152–5. doi:10.1103/PhysRevLett.38.152

52. Salvat F, Jablonski A, Powell CJ. Elsepa - Dirac partial-wave calculation of elastic scattering of electrons and positrons by atoms, positive ions and molecules. *Computer Phys Commun* (2005) 165:157–90. doi:10.1016/j.cpc.2004.09.006

53. Bender M, Heenen PH, Reinhard PG. Self-consistent mean-field models for nuclear structure. *Rev Mod Phys* (2003) 75:121–80. doi:10.1103/RevModPhys.75.121

54. Wang M, Huang W, Kondev F, Audi G, Naimi S. The ame 2020 atomic mass evaluation (ii). tables, graphs and references. *Chin Phys C* (2021) 45:030003. doi:10.1088/1674-1137/abddaf

55. Pruitt CD, Charity RJ, Sobotka LG, Atkinson MC, Dickhoff WH. Systematic matter and binding-energy distributions from a dispersive optical model analysis. *Phys Rev Lett* (2020) 125:102501. doi:10.1103/PhysRevLett.125.102501

56. Pruitt CD, Charity RJ, Sobotka LG, Elson JM, Hoff DEM, Brown KW, et al. Isotopically resolved neutron total cross sections at intermediate energies. *Phys Rev C* (2020) 102:034601. doi:10.1103/PhysRevC.102.034601

57. Anderson BD, Bevington PR, Cverna FH, McNaughton MW, Willard HB, Barrett RJ, et al. Proton total reaction cross section measurements for ^{40,44,48}Ca at 700 mev. *Phys Rev C* (1979) 19:905–12. doi:10.1103/PhysRevC.19.905

58. Lichtenstadt J, Heisenberg J, Papanicolas CN, Sargent CP, Courtemanche AN, McCarthy JS. High-spin states of J^{π} = 12−, 14− in ^{208}Pb studied by (e,e′). *Phys Rev C* (1979) 20:497–503. doi:10.1103/PhysRevC.20.497

59. Pandharipande VR, Papanicolas CN, Wambach J. Occupation probabilities of shell-model orbits in the lead region. *Phys Rev Lett* (1984) 53:1133–6. doi:10.1103/PhysRevLett.53.1133

60. Sick I, de Witt Huberts PKA. *Comm Nucl Part Phys* (1991) 20:177. Available online at: https://inspirehep.net/literature/1406038

61. Quint ENM, van den Brand JFJ, den Herder JWA, Jans E, Keizer PHM, Lapikás L, et al. Relative 3s spectroscopic strength in ^{206}Pb and ^{208}Pb studied with the (e, e $'$ p) knockout reaction. *Phys Rev Lett* (1986) 57:186–9. doi:10.1103/PhysRevLett.57.186

62. Quint ENM, Barnett BM, van den Berg AM, van den Brand JFJ, Clement H, Ent R, et al. Evidence for partial occupancy of the $3s_{1/2}$ proton orbit in ^{208}Pb. *Phys Rev Lett* (1987) 58:1088–91. doi:10.1103/PhysRevLett.58.1088

63. van Batenburg MF. Netherlands: Utrecht University (2001). *Ph.D. Thesis*.

64. Hen O, Miller GA, Piasetzky E, Weinstein LB. Nucleon-nucleon correlations, short-lived excitations, and the quarks within. *Rev Mod Phys* (2017) 89:045002. doi:10.1103/RevModPhys.89.045002

65. Egiyan KS, Dashyan NB, Sargsian MM, Strikman MI, Weinstein LB, Adams G, et al. Measurement of two- and three-nucleon short-range correlation probabilities in nuclei. *Phys Rev Lett* (2006) 96:082501. doi:10.1103/PhysRevLett.96.082501

66. Frick T, Müther H, Rios A, Polls A, Ramos A. Correlations in hot asymmetric nuclear matter. *Phys Rev C* (2005) 71:014313. doi:10.1103/PhysRevC.71.014313

67. Rios A, Polls A, Dickhoff WH. Depletion of the nuclear fermi sea. *Phys Rev C* (2009) 79:064308. doi:10.1103/PhysRevC.79.064308

68. Rios A, Polls A, Dickhoff WH. Density and isospin-asymmetry dependence of high-momentum components. *Phys Rev C* (2014) 89:044303. doi:10.1103/PhysRevC.89.044303

69. Duer M, Hen O, Piasetzky E, Hakobyan H, Weinstein LB, Braverman M, et al. Probing high-momentum protons and neutrons in neutron-rich nuclei. *Nature* (2018) 560:617–21. doi:10.1038/s41586-018-0400-z

70. Wiringa RB, Schiavilla R, Pieper SC, Carlson J. Nucleon and nucleon-pair momentum distributions in $a \leq 12$ nuclei. *Phys Rev C* (2014) 89:024305. doi:10.1103/PhysRevC.89.024305

71. Rohe D, Armstrong CS, Asaturyan R, Baker OK, Bueltmann S, Carasco C, et al. Correlated strength in the nuclear spectral function. *Phys Rev Lett* (2004) 93:182501. doi:10.1103/PhysRevLett.93.182501

72. Horowitz CJ, Kumar KS, Michaels R. Electroweak measurements of neutron densities in CREX and PREX at JLab, USA. *Eur Phys A* (2014) 50:48. doi:10.1140/epja/i2014-14048-3

73. Adhikari D, Albataineh H, Androic D, Aniol KA, Armstrong DS, Averett T, et al. Precision determination of the neutral weak form factor of ^{48}Ca. *Phys Rev Lett* (2022) 129:042501. doi:10.1103/PhysRevLett.129.042501

74. Adhikari D, Albataineh H, Androic D, Aniol K, Armstrong DS, Averett T, et al. Accurate determination of the neutron skin thickness of ^{208}Pb through parity-violation in electron scattering. *Phys Rev Lett* (2021) 126:172502. doi:10.1103/PhysRevLett.126.172502

75. Hicks SF, Hicks SE, Shen GR, McEllistrem MT. Collective doorway configurations in ^{49}Ca through neutron scattering on ^{48}Ca. *Phys Rev C* (1990) 41:2560–70. doi:10.1103/PhysRevC.41.2560

76. Harvey JA, Johnson CH, Carlton RF, Castel B. Single-particle $2d_{5/2}$ strength in the ^{48}ca+n reaction. *Phys Rev C* (1985) 32:1114–7. doi:10.1103/PhysRevC.32.1114

77. Shane R, Charity R, Elson J, Sobotka L, Devlin M, Fotiades N, et al. Total neutron cross-sections for rare isotopes using a digital-signal-processing technique: case study 48ca. *Nucl Instr Methods Phys Res Section A: Acc Spectrometers, Detectors Associated Equipment* (2010) 614:468–74. doi:10.1016/j.nima.2010.01.005

78. Abbott BP, Abbott R, Abbott T, Acernese F, Ackley K, Adams C, et al. Gw170817: observation of gravitational waves from a binary neutron star inspiral. *Phys Rev Lett* (2017) 119:161101. doi:10.1103/PhysRevLett.119.161101